

Extracting pairs of time-bin entangled photons from resonance fluorescence

Xin-Xin Hu, Gabriele Maron, Luke Masters, Arno Rauschenbeutel,^{*} and Jürgen Volz[†]

Department of Physics, Humboldt Universität zu Berlin, 10099 Berlin, Germany

(Dated: August 20, 2025)

Photon-photon entanglement and photon antibunching are fundamental manifestations of the quantum nature of optical light fields, but are typically regarded as distinct phenomena. Here, we experimentally demonstrate that pairs of narrow-band time-bin entangled photons can be naturally extracted from resonance fluorescence. We split the collected fluorescence of a single trapped atom on a 50 : 50 beamsplitter, resulting in strong temporal correlations between photons at the beamsplitter outputs. A time-bin coincidence between the two output modes then projects their state onto a maximally entangled Bell state. This entanglement is evidenced by violating the CHSH-Bell inequality as well as by reconstructing the density matrix of the photon pair. Importantly, we show that the entanglement persists both for weak and strong excitation of the emitter. Our results establish resonance fluorescence as an efficient source of time-bin entangled photon pairs, i.e., a practical and scalable resource for quantum communication and photonic quantum technologies.

Individually controlled two-level quantum systems can be realized using, e.g., laser-cooled atoms [1–6] or ions [7, 8], quantum dots [9, 10], single molecules [11–14] or defect centers [15–17]. They constitute an exceptional platform for applications in quantum information and communication as well as fundamental studies of quantum optics and quantum mechanics. Their well-defined energy structure, whose interaction with light is a fundamentally quantum mechanical phenomenon, underlies many emerging quantum information technologies, particularly for the realization of quantum light sources [18, 19].

When coherently driven by near-resonant light, such two-level emitters scatter photons, giving rise to so-called resonance fluorescence. The corresponding stream of photons displays hallmark quantum features such as photon antibunching, evidenced by a vanishing second-order correlation function at zero time-delay [20]. Although photon antibunching has been observed in many experiments, recent research efforts have been put into understanding and harnessing the physical process underlying its occurrence in resonance fluorescence [21–23]. In this context, it has been experimentally shown that antibunching arises from destructive quantum interference between the two-photon components of the so-called coherent and incoherent scattering processes. In particular, it has been shown that when removing the incoherent or the coherent component via spectral filtering, the remaining light field loses all photon correlations [23], or consists predominantly of photon pairs [24], respectively. Recently, pioneering works have experimentally confirmed the presence of energy-time entanglement in these photon pairs [25, 26]. As a consequence, selectively spectrally filtering resonance fluorescence constitutes a new and attractive avenue for generating entangled pairs of photons, complementing the more established methods of spontaneous parametric down-conversion [27–30],

four-wave mixing [31–34], or cascaded emission [35–37].

In this Letter, we show that resonance fluorescence without any spectral filtering, i.e., comprising the full Mollow spectrum, can be harnessed to generate narrow-band time-bin entangled pairs of photons. For this, we simply send the collected fluorescence of a single trapped atom onto a 50 : 50 beamsplitter, thereby generating two distinct spatial modes, which, however, feature strong temporal correlations due to the photon antibunching initially present. In particular, thanks to these correlations, a time-bin coincidence between the two spatial modes projects their state onto a maximally entangled Bell state. We verify this entanglement by violating a Clauser–Horne–Shimony–Holt (CHSH) type Bell inequality [38] as well as by reconstructing the density matrix through quantum state tomography. Our method thereby enables the generation of pairs of entangled photons whose frequency and bandwidth are ideally suited for interfacing with and storing in atom-based quantum memories for long-distance quantum communication.

To elucidate the origin of the entanglement, one has to consider that, light emitted by a single two-level quantum emitter under continuous and near-resonant coherent excitation exhibits photon antibunching. This means that at any given time of detection and distance from the atom, the fluorescence light contains, at most, a single photon. We now consider the situation in Fig. 1, where the fluorescence is sent onto a 50 : 50 beamsplitter. We refer to the beamsplitter outputs as modes a and b , respectively. We then assume that the four spatio-temporal modes described by the operators, $a_{t_1}^\dagger b_{t_1}^\dagger$, $a_{t_2}^\dagger b_{t_2}^\dagger$, $a_{t_1}^\dagger b_{t_2}^\dagger$ and $a_{t_2}^\dagger b_{t_1}^\dagger$ contain in total two photons. Here, $a_{t_1}^\dagger$ ($a_{t_2}^\dagger$) and $b_{t_1}^\dagger$ ($b_{t_2}^\dagger$) are the creation operators of a photon in mode a and b at time t_1 and t_2 . In this case, the light is described by the state

$$|\Psi\rangle \propto \psi(\tau) \left[a_{t_1}^\dagger b_{t_2}^\dagger + a_{t_2}^\dagger b_{t_1}^\dagger \right] |0\rangle + \psi(0) \left[a_{t_1}^\dagger b_{t_1}^\dagger + a_{t_2}^\dagger b_{t_2}^\dagger \right] |0\rangle. \quad (1)$$

Here, $\psi(\tau)$ and $\psi(0)$ are the amplitudes of having two fluorescence photons featuring a time delay $\tau = t_1 - t_2$

^{*} arno.rauschenbeutel@hu-berlin.de

[†] juergen.volz@hu-berlin.de

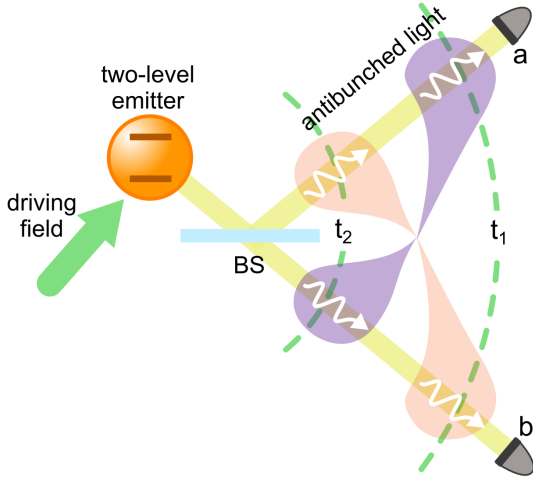


FIG. 1. Resonance-fluorescence-mediated entanglement. A single two-level quantum emitter, continuously driven by a coherent driving field, scatters light that features antibunched photon statistics, i.e., each emitted photon inhabits a temporally-distinct time-bin. Sending the emitted light onto a beamsplitter (BS), this absence of simultaneous photon emission ensures that one never observes a photon coincidence detection in the two output modes, a and b of the beamsplitter. When there is a photon in each output mode, the emitted light is then in the maximally entangled superposition state of: early emission into mode a and late emission into mode b (purple shaded), plus early emission into mode b and late emission into mode a (orange shaded).

and at zero time delay, respectively, see Supplementary Materials. In the case of uncorrelated light, $\psi(\tau) = \psi(0)$ and Eq. (1) corresponds to a separable state. For perfectly antibunched light, however, we have $|\psi(0)|^2 = 0$ and Eq. (1) corresponds to a maximally entangled Bell state. Remarkably, in the absence of external decoherence mechanisms, the entangled state described by Eq. (1) is valid for any time difference $\tau \neq 0$ and persists regardless of the driving strength. This is because the fundamental quantum interference that underlies photon antibunching ensures that the two-photon probability $|\psi(\tau = 0)|^2 = 0$, prevails for any excitation strength, i.e., from weak excitation through to large saturation, see Supplementary Materials.

To experimentally test the entanglement, we use a single trapped ^{85}Rb atom (Fig. 2a) that produces antibunched fluorescence light (Fig. 2b) and send it onto a beamsplitter that routes the photons to *Alice* and *Bob*, respectively. We transform the state in Eq. (1) into a readily experimentally detectable quantum state by employing a Franson-type interferometer setup (Fig. 2c). Each observer, *Alice* and *Bob*, uses an unbalanced Mach-Zehnder interferometer that exhibits a path delay $\Delta t_{A(B)} \approx 46$ ns, longer than the correlation time $\tau = (2\gamma)^{-1}$ of the antibunching, where $\tau = 26.5$ ns is the excited state lifetime of ^{85}Rb [39]. For photons that fulfill $|t_1 - t_2| = \Delta t$, the entangled state in Eq. (1) is thus

transformed into the two-mode entangled state

$$|\Psi_{\text{Bell}}\rangle = \frac{1}{\sqrt{2}} \left[a_s^\dagger(t) b_l^\dagger(t) + a_l^\dagger(t) b_s^\dagger(t) \right] |0\rangle, \quad (2)$$

where the path delay Δt sets the particular emission time difference $t_1 - t_2$ that we study. Here a_s^\dagger (b_s^\dagger) and a_l^\dagger (b_l^\dagger) are the creation operators of a photon in the short and long arm of *Alice's* (*Bob's*) interferometer, respectively. Equation (2) describes a maximally entangled Bell state. Its origin can intuitively be understood when considering that photons entering the Franson-type interferometer setup can take four possible path combinations, i.e., long-short $|l, s\rangle$, short-short $|s, s\rangle$, long-long $|l, l\rangle$, and short-long $|s, l\rangle$. However, photon antibunching ensures a temporal separation between the photons. This timing constraint suppresses the amplitudes for the states $|s, s\rangle$ and $|l, l\rangle$ and subsequently maps the initial entangled state in Eq. (1) to Eq. (2).

The Franson interferometer setup also allows a direct analysis of the entangled state in different measurement bases. For this purpose, we place phase shifters in the long arms of *Alice's* and *Bob's* interferometers, thereby setting the respective phases ϕ_A and ϕ_B . Recombining the modes at the output beamsplitters, the photons are routed into different output ports for which we assign a value of $+1$ to detections at port 1 (a_1 or b_1) and -1 to detections at port 2 (a_2 or b_2). In this way we can measure the expectation values $\langle \sigma_{\phi_A} \rangle$ and $\langle \sigma_{\phi_B} \rangle$, for the photons on *Alice's* and *Bob's* side respectively, where $\sigma_\phi = \cos \phi \sigma_x + \sin \phi \sigma_y$ and σ_x and σ_y are the Pauli matrices defined for the two-dimensional Hilbert space of the photon.

Scanning ϕ_A and ϕ_B and measuring the single photon expectation values $\langle \sigma_{\phi_A} \rangle$ and $\langle \sigma_{\phi_B} \rangle$ unveils single-photon interference fringes (Fig. 3) with visibilities that depend on the drive strength. Under weak excitation (saturation parameter $s_0 = 0.10$), we observe a visibility of $V_A = 92 \pm 1\%$ and $V_B = 93 \pm 1\%$, while driving the atom at high saturation intensity ($s_0 = 2.75$) leads to a decrease of the visibilities to $61.8 \pm 1\%$ and $63.4 \pm 1\%$. This behavior originates from the dual composition of resonance fluorescence, that has driving-dependent contributions of the coherent and incoherent scattering components [40]. Only the coherent component, that results from elastic photon-atom interactions and preserves the narrow linewidth of the excitation laser, exhibits a well-defined phase and thus high-contrast interference fringes. In comparison, the incoherently scattered component exhibits a broader spectral linewidth ($\delta\omega \geq 2\gamma$) and thus gives rise to a reduced interference contrast for an interferometric delay $\Delta t > (2\gamma)^{-1}$ as in our case. As the ratio of coherent to incoherent scattering decreases with increasing saturation, the interference visibility correspondingly diminishes, see Supplementary Materials for more details.

Next, in order to quantify the amount of entanglement in the photon pairs, we study the violation of a CHSH-

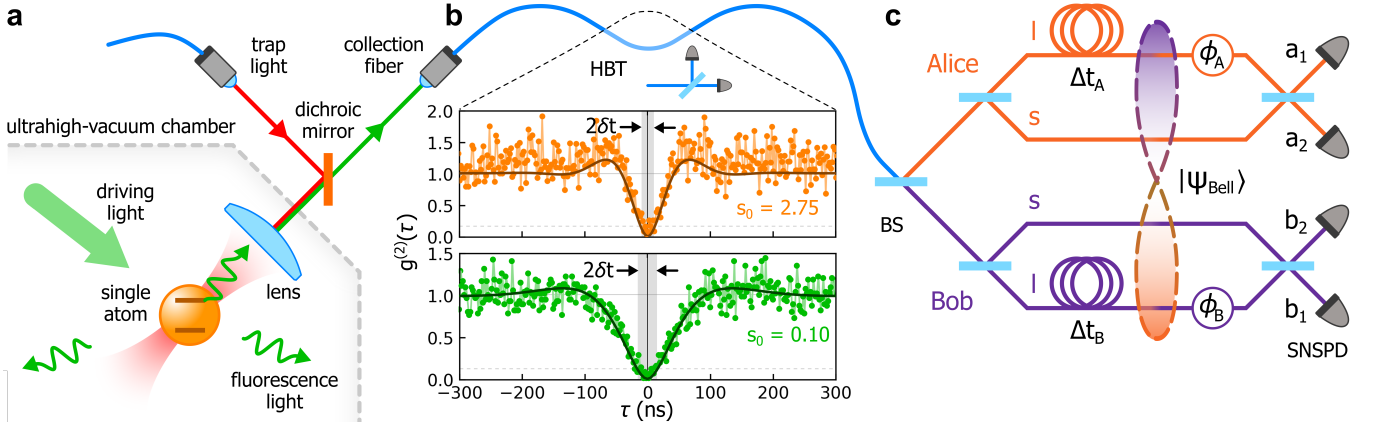


FIG. 2. Experimental set-up. **a**, A single two-level atom is loaded from a MOT into an optical dipole trap, and resonantly driven by an external laser with a residual detuning of $\Delta = 2\pi \times (2.56 \pm 0.16)$ MHz. Fluorescence photons from the trapped atom are collected using a high numerical aperture lens (NA = 0.55) and coupled into a single-mode fiber. **b**, Second-order correlation functions ($g^{(2)}(\tau)$) of the collected fluorescence measured under different driving regimes. Clear antibunching is evident in the photon statistics in both the low and high driving regimes (respectively green and orange). The dark solid curves are theoretical fits, see Supplementary Materials. The shaded region indicates the variable-width coincidence window, δt used for the Bell-inequality violation. **c**, A 50:50 beamsplitter (BS) equally splits up the collected fluorescence and sends it into an all-fiber-based Franson-type setup, consisting of an unbalanced Mach-Zehnder interferometer on *Alice's* (orange) and *Bob's* (purple) side, respectively. Each of these has a long (l) and short (s) arm, with a delay time of $\Delta t_{A(B)}$. The path length difference is stabilized and set to impart a relative phase $\phi_{A(B)}$. Photons are detected in the output of each interferometer using superconducting nanowire single-photon detectors (SNSPD), and their coincidence detection results in a maximally entangled Bell state, $|\Psi_{\text{Bell}}\rangle$.

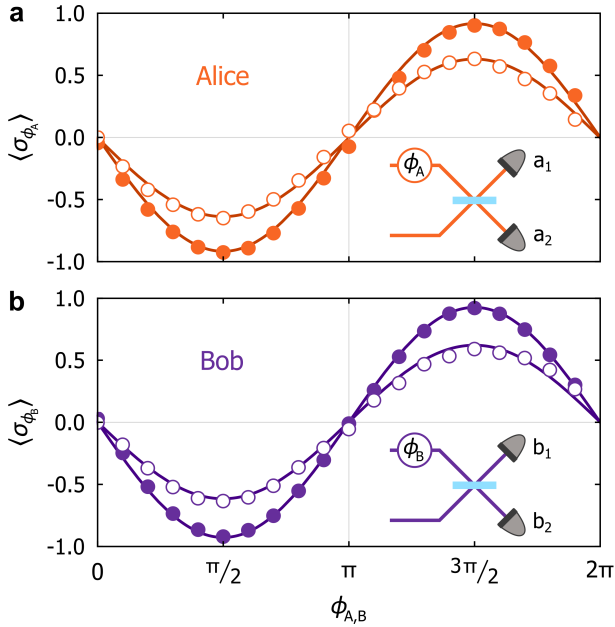


FIG. 3. Single photon visibility. Measured expectation values, $\langle \sigma_{\phi_A} \rangle$ and $\langle \sigma_{\phi_B} \rangle$, obtained when launching resonance fluorescence through **a** *Alice's* and **b** *Bob's* interferometer for different phases ϕ_A and ϕ_B , respectively. Sinusoidal fits (solid lines) to the data yield visibilities of $V_A = 92 \pm 1\%$ and $V_B = 93 \pm 1\%$ for low saturation (solid circles), and $V_A = 61.8 \pm 1\%$ and $V_B = 63.4 \pm 1\%$ for high saturation (open circles). The 1σ error bars are smaller than the displayed data points.

type Bell inequality [38] by measuring the S -parameter

$$S = |\langle \sigma_{\phi_A} \sigma_{\phi_B} \rangle + \langle \sigma_{\phi_{A'}} \sigma_{\phi_B} \rangle - \langle \sigma_{\phi_A} \sigma_{\phi_{B'}} \rangle + \langle \sigma_{\phi_{A'}} \sigma_{\phi_{B'}} \rangle|. \quad (3)$$

Using optimal phase settings $\phi_A = 0$, $\phi_{A'} = \frac{\pi}{2}$, $\phi_B = \frac{\pi}{4}$ and $\phi_{B'} = \frac{3\pi}{4}$, the sum of the joint expectation values should reach $S = 2\sqrt{2} \approx 2.828$ for a maximally entangled state. Figure 4a shows the measured two-photon expectation values for our phase settings under both low- and high-saturation regimes, using a coincidence window of $\delta t = \pm 10$ ns (for $s_0 = 0.10$) and $\delta t = \pm 3$ ns (for $s_0 = 2.75$) as depicted in Fig. 2b [41]. We measure $S = 2.80 \pm 0.19$ and $S = 2.55 \pm 0.22$ in the low and high-saturation regimes, respectively. This corresponds to a 4.2σ and 2.5σ violation of the local realistic boundary of $S \leq 2$ and clearly shows the high degree of entanglement of the measured photon pairs.

The measured entanglement depends on the coincidence window width δt , as the required photon antibunching decreases with increasing temporal integration window. To analyze this, we measure the dependence of S on the width of the coincidence window δt , see Fig. 4. For both driving strengths, we measure $S > 2$ up to a time window δt_{max} for which $g^{(2)}(|\tau| = \delta t_{\text{max}}) \approx 0.4$. For weak driving, this yields $\delta t_{\text{max}} \approx \pm 30$ ns close to the atomic lifetime. At strong driving, however, this threshold reduces to $\delta t_{\text{max}} \approx \pm 17$ ns, confirming the necessity of photon antibunching to observe entanglement. For larger time windows, S decays toward values characteristic of uncorrelated photons, see Supplementary Mate-

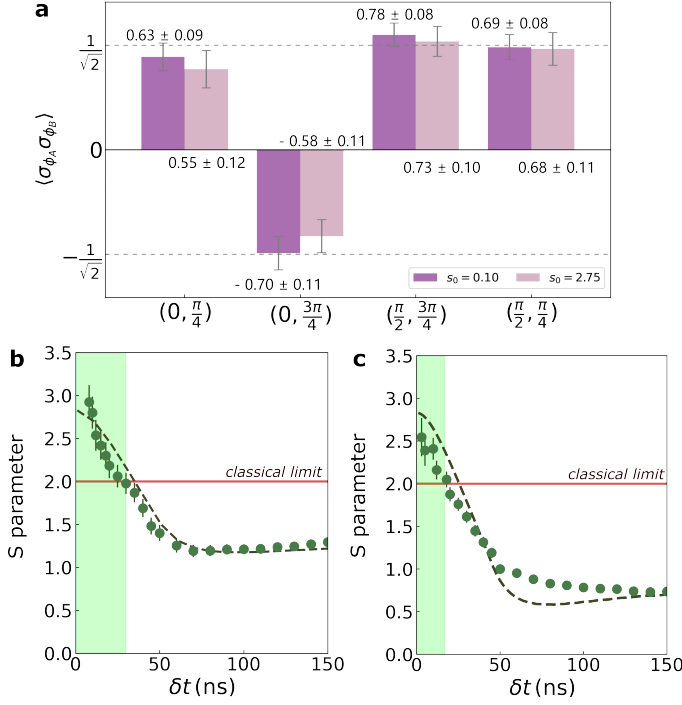


FIG. 4. Violating the CHSH inequality with resonance fluorescence. **a**, Measured two-photon correlations of the outputs of Alice’s and Bob’s interferometer for different settings of the phases ϕ_A and ϕ_B . From these correlations, we deduce S -parameters of $S = 2.80 \pm 0.19$ for low saturation and $S = 2.55 \pm 0.22$ for high saturation. **b** and **c**, Measured S -parameter (green dots) as a function of the coincidence time window, δt . The dashed line shows the theoretical prediction. For δt within the green-shaded area, the measured S -parameters violate the CHSH inequality (horizontal red line). For larger δt , S approaches the characteristic level of uncorrelated photons.

rials.

To further quantify the photon-photon entangled state, we perform a tomographic reconstruction of its density matrix ρ for the weak excitation regime, see Supplementary Materials for details. Figure 5 shows the reconstructed matrix for a $\delta t = \pm 10$ ns coincidence window. Calculating the overlap between the measured density matrix ρ and the expected Bell state, we find a fidelity of $F = \langle \Psi_{\text{Bell}} | \rho | \Psi_{\text{Bell}} \rangle = 0.87 \pm 0.02$, which again illustrates the high degree of entanglement of the two-photon state. Using the Peres–Horodecki criterion [42] we can calculate the expected CHSH-inequality violation for the measured density matrix and obtain $S_F = 2.57 \pm 0.05$, in agreement with the direct measurement of S above.

Both measurements, quantum state-tomography and Bell-inequality violation confirm the presence of high-fidelity entanglement. We note that our results are obtained with unmodified resonance fluorescence photons, unlike in approaches that reject coherent scattering via spectral filtering [25, 26], or employ fully incoherent ex-

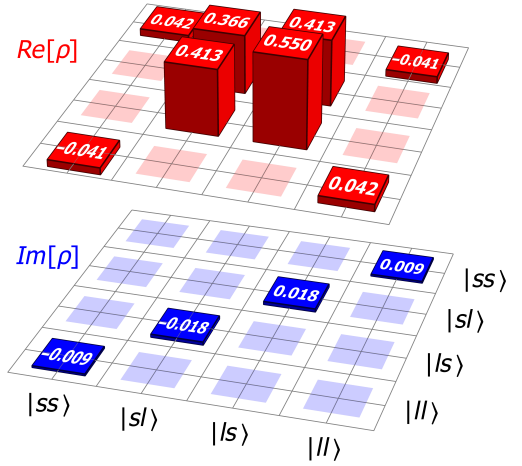


FIG. 5. Tomographically reconstructed density matrix. The real (red) and imaginary (blue) parts of $\rho = |\Psi_{\text{Bell}}\rangle\langle\Psi_{\text{Bell}}|$ measured in a $\delta t = \pm 10$ ns coincidence window centred at zero time delay. Non-zero entries are labeled accordingly.

citation [13, 14]. Furthermore, in contrast to the works presented in [25, 26], our scheme is not limited to weak driving, in the sense that increasing the pair rate via an increased drive strength ideally does not come at the expense of a reduction of the entanglement fidelity.

Interestingly, in addition to the entanglement, we also observe strong single photon coherence as validated by the high visibility of the interference fringes of the individual interferometers in Fig. 3. In order to understand how resonance fluorescence can simultaneously feature entanglement and single photon coherence one has to look in more detail at their physical origin. The high visibility observed in Fig. 3 under low saturation stems from the predominance of coherently scattered light in the resonance fluorescence with its well defined coherence properties. In contrast to this, the entanglement properties are inherently linked to the nonclassical photon statistics of the light and thus to the destructive quantum interference of the coherent and incoherent components [24]. As this interference prevails over all drive strengths of the emitter, one expects no change of entanglement with increasing saturation while the coherent component decreases, and thus the single photon visibility reduces. However, the maximum entangled photon pair rate that can be measured depends on saturation as it is given by a trade-off between photon flux and the limited duration of photon antibunching. A maximum pair rate of about 2% of the maximum single-photon scattering rate γ should be achieved at $s_0 = 4$, see Supplementary Materials.

In conclusion, we have experimentally demonstrated that entangled photon pairs can be extracted from resonance fluorescence from a single quantum emitter. Using a Franson-type setup, we transform the entangled state into a maximally time-bin entangled Bell state. We note that, in other entanglement procedures, such as nonlinear parametric down-conversion or four-wave mixing, the

pair photons are generated simultaneously and it is this generation process that gives rise to the entanglement. In contrast, in our approach, the photons are generated independently and the entanglement stems from the indistinguishability of the photons in conjunction with the anticorrelations in the emission statistics of the two-level emitter. Their narrow bandwidth, inherently compatible with the emitter's linewidth, renders this process ideal for interfacing atomic quantum memories, a critical component for scalable quantum communication. Our scheme can also be realized with other two-level quantum emitters capable of generating indistinguishable photons. In this context, a small dephasing rate and a correspondingly large antibunching time turn out advantageous because they allow for larger coincidence time windows and, consequently, higher coincidence rates. Furthermore, beyond single emitters, any first-order coherent source exhibiting antibunching [43, 44] can be harnessed for the generation of entangled photon pairs using the presented

method. Future work could extend this scheme for the generation of higher-dimensional entanglement looking for example at three photon coincidences.

ACKNOWLEDGMENTS

We acknowledge stimulating discussions with Anders S. Sørensen and Martin Cordier and funding by the Alexander von Humboldt Foundation in the framework of the Alexander von Humboldt Professorship endowed by the Federal Ministry of Education and Research, as well as by the European Commission under the project DAALI (No.899275). X.-X. H. acknowledges a Humboldt Research Fellowship by the Alexander von Humboldt Foundation.

-
- [1] W. D. Phillips, Nobel lecture: Laser cooling and trapping of neutral atoms, *Rev. Mod. Phys.* **70**, 721 (1998).
 - [2] N. Schlosser, G. Reymond, I. Protsenko, and P. Grangier, Sub-poissonian loading of single atoms in a microscopic dipole trap, *Nature* **411**, 1024 (2001).
 - [3] M. Endres, H. Bernien, A. Keesling, H. Levine, E. R. Anschuetz, A. Krajenbrink, C. Senko, V. Vuletic, M. Greiner, and M. D. Lukin, Atom-by-atom assembly of defect-free one-dimensional cold atom arrays, *Science* **354**, 1024 (2016).
 - [4] D. Barredo, V. Lienhard, S. de Léséleuc, T. Lahaye, and A. Browaeys, Synthetic three-dimensional atomic structures assembled atom by atom, *Nature* **561**, 79 (2018).
 - [5] I. Bloch, J. Dalibard, and W. Zwerger, Many-body physics with ultracold gases, *Rev. Mod. Phys.* **80**, 885 (2008).
 - [6] A. M. Kaufman, B. J. Lester, C. M. Reynolds, M. L. Wall, M. Foss-Feig, K. R. A. Hazzard, A. M. Rey, and C. A. Regal, Two-particle quantum interference in tunnel-coupled optical tweezers, *Science* **345**, 306 (2014).
 - [7] C. Monroe and J. Kim, Scaling the ion trap quantum processor, *Science* **339**, 1164 (2013).
 - [8] H. Häffner, C. Roos, and R. Blatt, Quantum computing with trapped ions, *Physics Reports* **469**, 155 (2008).
 - [9] C. Kloeffer and D. Loss, Prospects for spin-based quantum computing in quantum dots, *Annual Review of Condensed Matter Physics* **4**, 51 (2013).
 - [10] D. Fattal, K. Inoue, J. Vuckovic, C. Santori, G. S. Solomon, and Y. Yamamoto, Entanglement formation and violation of bell's inequality with a semiconductor single photon source, *Phys. Rev. Lett.* **92**, 037903 (2004).
 - [11] L. Anderegg, L. W. Cheuk, Y. Bao, S. Burchesky, W. Ketterle, K.-K. Ni, and J. M. Doyle, An optical tweezer array of ultracold molecules, *Science* **365**, 1156 (2019).
 - [12] C. Toninelli, I. Gerhardt, A. S. Clark, A. Reserbat-Plantey, S. Götzinger, Z. Ristanović, M. Colautti, P. Lombardi, K. D. Major, I. Deperasińska, W. H. Pernice, F. H. L. Koppens, B. Kozankiewicz, A. Gourdon, V. Sandoghdar, and M. Orrit, Single organic molecules for photonic quantum technologies, *Nature Materials* **20**, 1615 (2021).
 - [13] J.-B. Trebbia, P. Tamarat, and B. Lounis, Indistinguishable near-infrared single photons from an individual organic molecule, *Phys. Rev. A* **82**, 063803 (2010).
 - [14] M. Rezai, J. Wrachtrup, and I. Gerhardt, Polarization-entangled photon pairs from a single molecule, *Optica* **6**, 34 (2019).
 - [15] D. D. Awschalom, R. Hanson, J. Wrachtrup, and B. B. Zhou, Quantum technologies with optically interfaced solid-state spins, *Nature Photonics* **12**, 516 (2018).
 - [16] N. P. de Leon, K. M. Itoh, D. Kim, K. K. Mehta, T. E. Northup, H. Paik, B. S. Palmer, N. Samarth, S. Sangtawesin, and D. W. Steuerman, Materials challenges and opportunities for quantum computing hardware, *Science* **372**, eabb2823 (2021).
 - [17] T. Schröder, M. E. Trusheim, M. Walsh, L. Li, J. Zheng, M. Schukraft, A. Sipahigil, R. E. Evans, D. D. Sukachev, C. T. Nguyen, J. L. Pacheco, R. M. Camacho, E. S. Bielejec, M. D. Lukin, and D. Englund, Scalable focused ion beam creation of nearly lifetime-limited single quantum emitters in diamond nanostructures, *Nature Communications* **8**, 15376 (2017).
 - [18] I. Aharonovich, D. Englund, and M. Toth, Solid-state single-photon emitters, *Nature Photonics* **10**, 631 (2016).
 - [19] N. Somaschi, V. Giesz, L. De Santis, J. C. Lored, M. P. Almeida, G. Hornecker, S. L. Portalupi, T. Grange, C. Antón, J. Demory, C. Gómez, I. Sagnes, N. D. Lanzillotti-Kimura, A. Lemaître, A. Auffèves, A. G. White, L. Lanco, and P. Senellart, Near-optimal single-photon sources in the solid state, *Nature Photonics* **10**, 340 (2016).
 - [20] H. J. Kimble, M. Dagenais, and L. Mandel, Photon antibunching in resonance fluorescence, *Phys. Rev. Lett.* **39**, 691 (1977).
 - [21] E. del Valle, A. Gonzalez-Tudela, F. P. Laussy, C. Tejedor, and M. J. Hartmann, Theory of frequency-filtered and time-resolved n -photon correlations, *Phys. Rev. Lett.*

- 109, 183601 (2012).**
- [22] C. L. Phillips, A. J. Brash, D. P. S. McCutcheon, J. Iles-Smith, E. Clarke, B. Royall, M. S. Skolnick, A. M. Fox, and A. Nazir, Photon statistics of filtered resonance fluorescence, *Phys. Rev. Lett.* **125**, 043603 (2020).
 - [23] L. Hanschke, L. Schweickert, J. C. L. Carreño, E. Schöll, K. D. Zeuner, T. Lettner, E. Z. Casalengua, M. Reindl, S. F. C. da Silva, R. Trotta, J. J. Finley, A. Rastelli, E. del Valle, F. P. Laussy, V. Zwiller, K. Müller, and K. D. Jöns, Origin of antibunching in resonance fluorescence, *Phys. Rev. Lett.* **125**, 170402 (2020).
 - [24] L. Masters, X.-X. Hu, M. Cordier, G. Maron, L. Pache, A. Rauschenbeutel, M. Schemmer, and J. Volz, On the simultaneous scattering of two photons by a single two-level atom, *Nat. Photon.* **17**, 972 (2023).
 - [25] S. Liu, O. A. D. Sandberg, M. L. Chan, B. Schirnski, Y. Anyfantaki, R. B. Nielsen, R. G. Larsen, A. Skalkin, Y. Wang, L. Midolo, S. Scholz, A. D. Wieck, A. Ludwig, A. S. Sørensen, A. Tiranov, and P. Lodahl, Violation of bell inequality by photon scattering on a two-level emitter, *Nat. Phys.* **20**, 1429 (2024).
 - [26] J. Wang, X.-L. Zhou, Z.-M. Shen, D.-Y. Huang, S.-J. He, Q.-Y. Huang, Y.-J. Liu, C.-F. Li, and G.-C. Guo, Purcell-enhanced generation of photonic bell states via the inelastic scattering off single atoms, *Phys. Rev. Lett.* **134**, 053401 (2025).
 - [27] P. G. Kwiat, K. Mattle, H. Weinfurter, A. Zeilinger, A. V. Sergienko, and Y. Shih, New high-intensity source of polarization-entangled photon pairs, *Phys. Rev. Lett.* **75**, 4337 (1995).
 - [28] R. Valivarthi, M. G. Puigibert, Q. Zhou, G. H. Aguilar, V. B. Verma, F. Marsili, M. D. Shaw, S. W. Nam, D. Oblak, and W. Tittel, Quantum teleportation across a metropolitan fibre network, *Nat. Photon.* **10**, 676 (2016).
 - [29] X.-L. Wang, L.-K. Chen, W. Li, H.-L. Huang, C. Liu, C. Chen, Y.-H. Luo, Z.-E. Su, D. Wu, Z.-D. Li, H. Lu, Y. Hu, X. Jiang, C.-Z. Peng, L. Li, N.-L. Liu, Y.-A. Chen, C.-Y. Lu, and J.-W. Pan, Experimental ten-photon entanglement, *Phys. Rev. Lett.* **117**, 210502 (2016).
 - [30] A. Mataji-Kojouri and M. Liscidini, Narrow-band photon pair generation through cavity-enhanced spontaneous parametric down-conversion, *Phys. Rev. A* **108**, 053714 (2023).
 - [31] Q. Lin, F. Yaman, and G. P. Agrawal, Photon-pair generation in optical fibers through four-wave mixing: Role of raman scattering and pump polarization, *Phys. Rev. A* **75**, 023803 (2007).
 - [32] J. W. Silverstone, D. Bonneau, K. Ohira, N. Suzuki, H. Yoshida, N. Iizuka, M. Ezaki, C. M. Natarajan, M. G. Tanner, R. H. Hadfield, V. Zwiller, G. D. Marshall, J. G. Rarity, J. L. O'Brien, and M. G. Thompson, On-chip quantum interference between silicon photon-pair sources, *Nat. Photon.* **8**, 104 (2014).
 - [33] J. E. Sharping, K. F. Lee, M. A. Foster, A. C. Turner, B. S. Schmidt, M. Lipson, A. L. Gaeta, and P. Kumar, Generation of correlated photons in nanoscale silicon waveguides, *Opt. Express* **14**, 12388 (2006).
 - [34] K. Harada, H. Takesue, H. Fukuda, T. Tsuchizawa, T. Watanabe, K. Yamada, Y. Tokura, and S. Itabashi, Indistinguishable photon pair generation using two independent silicon wire waveguides, *New J. Phys.* **13**, 065005 (2011).
 - [35] A. Dousse, J. Suffczyński, A. Beveratos, O. Krebs, A. Lemaître, I. Sagnes, J. Bloch, P. Voisin, and P. Senellart, Ultrabright source of entangled photon pairs, *Nature* **466**, 217 (2010).
 - [36] M. Müller, S. Bounouar, K. D. Jöns, M. Glässl, and P. Michler, On-demand generation of indistinguishable polarization-entangled photon pairs, *Nature Photonics* **8**, 224 (2014).
 - [37] R. Trotta, J. Martín-Sánchez, J. S. Wildmann, G. Piredda, M. Reindl, C. Schimpf, E. Zallo, S. Stroj, J. Edlinger, and A. Rastelli, Wavelength-tunable sources of entangled photons interfaced with atomic vapours, *Nature Communications* **7**, 10375 (2016).
 - [38] J. F. Clauser, M. A. Horne, A. Shimony, and R. A. Holt, Proposed experiment to test local hidden-variable theories, *Phys. Rev. Lett.* **23**, 880 (1969).
 - [39] D. A. Steck, Rubidium 85 D line data, (Revision 2.3.3, 28 May 2024), available online at <http://steck.us/alkalidata>.
 - [40] C. Cohen-Tannoudji, B. Diu, and F. Laloe, *Quantum Mechanics* (Wiley, 2019).
 - [41] This time window was chosen by the condition that the theoretically expected second order correlation $g^{(2)}(\delta t) \approx 0.15$ and thus should yield the same quality of entanglement for both driving strengths.
 - [42] R. Horodecki, P. Horodecki, and M. Horodecki, Violating bell inequality by mixed spin-12 states: necessary and sufficient condition, *Phys. Lett. A* **200**, 340 (1995).
 - [43] A. S. Prasad, J. Hinney, S. Mahmoodian, K. Hammerer, S. Rind, P. Schneeweiss, A. S. Sørensen, J. Volz, and A. Rauschenbeutel, Correlating photons using the collective nonlinear response of atoms weakly coupled to an optical mode, *Nat. Photonics* **14**, 719–722 (2020).
 - [44] M. Cordier, M. Schemmer, P. Schneeweiss, J. Volz, and A. Rauschenbeutel, Tailoring photon statistics with an atom-based two-photon interferometer, *Phys. Rev. Lett.* **131**, 183601 (2023).
 - [45] D. A. Steck, *Quantum and Atom Optics* (Open Publication License, 2007).
 - [46] For our experiment, the condition $\Delta t \gg (2\gamma)^{-1}$ is not completely fulfilled giving rise to a residual single photon visibility also for incoherent photons.
 - [47] N. Schlosser, G. Reymond, and P. Grangier, Collisional blockade in microscopic optical dipole traps, *Phys. Rev. Lett.* **89**, 023005 (2002).
 - [48] K. Banaszek, G. M. D'Ariano, M. G. A. Paris, and M. F. Sacchi, Maximum-likelihood estimation of the density matrix, *Phys. Rev. A* **61**, 010304 (1999).
 - [49] D. F. V. James, P. G. Kwiat, W. J. Munro, and A. G. White, Measurement of qubits, *Phys. Rev. A* **64**, 052312 (2001).

SUPPLEMENTARY MATERIALS

A. Theoretical model

In the following, we consider the case of continuous driving of the atom with a coherent light field. For a given time duration, we can expand the scattered light field in terms of its photon number components as

$$|\psi\rangle = |0\rangle + \alpha|1\rangle + \beta|2\rangle + \dots \quad (4)$$

where $|1\rangle$ and $|2\rangle$ denote the number of photons in the scattered field and are given by

$$|1\rangle = \int dt a^\dagger(t) |0\rangle \quad (5)$$

$$|2\rangle = \iint dt d\tau \psi(\tau) a^\dagger(t) a^\dagger(t+\tau) |0\rangle. \quad (6)$$

Here, $a^\dagger(t)$ is the operator for the creation of a photon at time t . Note that $|2\rangle$ is not a Fock state but contains temporal fluctuations that are described by the two-photon wave function $\psi(\tau)$, which in the case of weak driving can be explicitly written as [24]

$$\psi(\tau) = 1 - e^{-(\gamma - i\Delta)|\tau|}, \quad (7)$$

related to $g^{(2)}(\tau) = |\psi(\tau)|^2$ in the chosen time window. After their generation and collection, the photons pass a first beamsplitter that directs them to *Alice* and *Bob*, as indicated by the operators $a^\dagger(t)$ and $b^\dagger(t)$, respectively. The corresponding two-photon state after the beam splitter is given by

$$\frac{1}{2} \iint dt d\tau \psi(\tau) a^\dagger(t) b^\dagger(t+\tau), \quad (8)$$

where the factor $1/2$ comes from the fact that we limit the discussion to the case where the two photons separate. The state in Eq. (1) can be derived from this expression by accordingly choosing the times t_1 and $t_2 = t_1 - \tau$. At *Alice* and *Bob*, a second beamsplitter sends each photon into the short or long arm, introducing a propagation delay Δt_A at *Alice* and Δt_B at *Bob*, respectively. Assuming that both interferometers exhibit the same path length difference $\Delta t = \Delta t_A = \Delta t_B$, the state in Eq. (8) is transformed such that the integrand reads

$$\begin{aligned} \frac{1}{2} \psi(\tau) & \left[a_s^\dagger(t) b_s^\dagger(t+\tau) + a_s^\dagger(t) b_l^\dagger(t+\tau+\Delta t) + \right. \\ & \left. a_l^\dagger(t+\Delta t) b_s^\dagger(t+\tau) + a_l^\dagger(t+\Delta t) b_l^\dagger(t+\tau+\Delta t) \right]. \end{aligned} \quad (9)$$

Here, the subscripts s and l denote the short and long interferometer arms, respectively. As we assume an experiment with a continuous and coherent driving of the atom, the scattered photons are indistinguishable such that in Eq. (9) only time differences between photons

matter. Consequently, the terms in the integrand can also be written as

$$\begin{aligned} \frac{1}{2} & \left[\psi(\tau) a_s^\dagger(t) b_s^\dagger(t+\tau) + \psi(\tau - \Delta t) a_s^\dagger(t) b_l^\dagger(t+\tau) \right. \\ & \left. + \psi(\tau + \Delta t) a_l^\dagger(t) b_s^\dagger(t+\tau) + \psi(\tau) a_l^\dagger(t) b_l^\dagger(t+\tau) \right] \quad (10) \end{aligned}$$

In the experiment, we are interested in the cases where *Alice* and *Bob* detect a photon coincidence with a small time delay $\delta t \ll \Delta t$, for which $\psi(\delta t) \approx 0$. For large delay times $\Delta t \geq (2\gamma)^{-1}$, the wavefunction does not vary much, so we can approximate $\psi(\Delta t + \tau) \approx \psi(\Delta t)$ and due to the time symmetry $\psi(\tau) = \psi(-\tau)$, Eq. (10) simplifies to

$$\begin{aligned} \frac{1}{2} \psi(\Delta t) & \left[a_s^\dagger(t) b_l^\dagger(t) + a_l^\dagger(t) b_s^\dagger(t) \right] + \\ \frac{1}{2} \psi(\delta t) & \left[a_s^\dagger(t) b_s^\dagger(t) + a_l^\dagger(t) b_l^\dagger(t) \right]. \end{aligned} \quad (11)$$

In the case of perfect antibunching and $\delta t \approx 0$, only the first part in the above expression remains. We thus obtain the maximally entangled Bell state given by Eq. (2) in the manuscript.

To measure the entanglement, we include a phase shifter that adds a phase shift ϕ_A and ϕ_B in the long arm of *Alice*'s and *Bob*'s interferometer, respectively, before closing them using another beamsplitter. Assigning the values ± 1 to the photon detections in the interferometer outputs, we can in this way measure the expectation values of the Pauli matrices $\langle \sigma_{\phi_{A(B)}} \rangle$ for the individual interferometers as well as the for the joint expectation values $\langle \sigma_{\phi_A} \sigma_{\phi_B} \rangle$ where $\sigma_\phi = \cos \phi \sigma_x + \sin \phi \sigma_y$, see section B. Using $g^{(2)}(\tau) = |\psi(\tau)|^2$, we get for the expectation value of the joint measurement $\langle \sigma_{\phi_A} \sigma_{\phi_B} \rangle$ for two photons with time delay δt

$$\begin{aligned} \langle \sigma_{\phi_A} \sigma_{\phi_B} \rangle &= \frac{g^{(2)}(\Delta t)}{g^{(2)}(\delta t) + g^{(2)}(\Delta t)} \cos(\phi_A - \phi_B) + \\ & \frac{g^{(2)}(\delta t)}{g^{(2)}(\delta t) + g^{(2)}(\Delta t)} \cos(\phi_A + \phi_B). \end{aligned} \quad (12)$$

From this expression, we get the limiting cases

$$\begin{aligned} \langle \sigma_{\phi_A} \sigma_{\phi_B} \rangle &\propto \cos(\phi_A - \phi_B) & (\delta t \approx 0) \\ &\propto \cos \phi_A \cos \phi_B. & (\delta t \gg \Delta t) \end{aligned} \quad (13)$$

Here, the first expression gives the expectation value for a maximally entangled state, while the second describes that of a fully separable state that is reached when the photons are detected with a large time delay. Equation (12) also shows that the degree of entanglement of the final state is directly related to the quality of antibunching, i.e., $g^{(2)}(0)$, that can be reached in the experiment.

To quantify the strength of the observable entanglement signature, we consider the S-parameter of the CHSH-Bell inequality as defined in Eq. (3). For the phase

settings in the experiment, it reaches the maximum possible value S_{max} . Using Eq. (12), this maximum can be expressed as

$$S_{max} = 2\sqrt{2} \frac{g^{(2)}(\Delta t)}{g^{(2)}(\delta t) + g^{(2)}(\Delta t)}. \quad (14)$$

The violation of the Bell inequality requires $S_{max} \geq 2$. Assuming sufficiently large delay times Δt such that $g^{(2)}(\Delta t) \approx 1$, this allows one to derive a condition on the quality of the antibunching that is required to observe a Bell-inequality violation at all

$$g^{(2)}(0) \leq \sqrt{2} - 1 \approx 0.414. \quad (15)$$

We note that throughout these derivations we made a weak driving approximation which allowed us to truncate the photon Hilbert space at two photons and to give an explicit expression for the two-photon wavefunction $\psi(\tau)$. However, for the case of sufficiently small time windows δt , we can always perform the state expansion to up to 2nd order in photon number such that Eq. (12) also applies in strong driving cases as long as δt is sufficiently small. Consequently, for $\delta t \approx 0$, Eq. (14) applies for arbitrary strong driving, thereby illustrating that the maximum entanglement fidelity does not depend on the drive strength.

In order to obtain a theoretical prediction of the influence of the size of the time window δt on the value of S , one has to average Eq. (14) over all values of δt in the coincidence window. The average value of S that is obtained in this way, is plotted as the black curve in Fig. 4. We note that for arbitrary δt , Eq. (14) is strictly only valid in the low driving regime. As our theoretical model does not provide an explicit expression similar to Eq. (14) for higher driving. In order to approximate the expected behavior, we by assume that the entanglement will show a similar decrease of S with increasing δt as for small drive strengths, however, we take into account the high saturation by scale the decay such that for large δt it approaches the steady state value calculated for independent photons for the given drive strengths, see section C.

B. Measurement of photon states

To measure the quantum state of the photons at *Alice* and *Bob*, we include a phase shifter that adds the phase shifts ϕ_A and ϕ_B in the long arm of each interferometer. Together with the final beamsplitter of the interferometer, this performs the transformation

$$c_s^\dagger \rightarrow \frac{1}{\sqrt{2}}(c_1^\dagger + c_2^\dagger) \quad (16)$$

$$c_l^\dagger \rightarrow \frac{e^{i\phi}}{\sqrt{2}}(c_1^\dagger - c_2^\dagger), \quad (17)$$

where $c_{s(l)}$ stands for $a_{s(l)}$ and $b_{s(l)}$, and the operators and $c'_{1(2)}$ define *Alice's* and *Bob's* output modes $a'_{1(2)}$

and $b'_{1(2)}$, respectively. Consequently, detecting a photon in the output $c'_{1,2}$ corresponds to detection of the state $(c_s^\dagger \pm e^{-i\phi} c_l^\dagger)/\sqrt{2}$, where $\phi \in \{\phi_A, \phi_B\}$. Assigning the values ± 1 to the detection events $c'_{1,2}$, this corresponds to a measurement of the Pauli matrices in the basis, $\langle \sigma_\phi \rangle = \langle \cos \phi \sigma_x + \sin \phi \sigma_y \rangle$, where σ_x and σ_y are the Pauli matrices in x - and y -direction.

Experimentally, the expectation values can be calculated via

$$\langle \sigma_{\phi_{A(B)}} \rangle = \frac{n_{a_1(b_1)} - n_{a_1(b_2)}}{n_{a_1(b_1)} + n_{a_1(b_2)}}, \quad (18)$$

where $n_{a_1(b_1)}$ ($n_{a_2(b_2)}$) is the number of detected photons in each output port. For the coincidence measurement between *Alice* and *Bob*, the joint expectation values can be calculated according to

$$\langle \sigma_{\phi_A} \sigma_{\phi_B} \rangle = \frac{n_{a_1,b_1} + n_{a_2,b_2} - n_{a_1,b_2} - n_{a_2,b_1}}{n_{a_1,b_1} + n_{a_2,b_2} + n_{a_1,b_2} + n_{a_2,b_1}}, \quad (19)$$

where $n_{a_1(2),b_1(2)}$ is the number of detected coincidences between the different detectors.

C. Coherence properties and rate of single photons

In our experiment, we observe simultaneously single photon coherence of the fluorescence light as illustrated in the interference pattern shown in Fig. 3, as well as coherence of the two-photon state which manifests itself as correlations between *Alice* and *Bob*. To get a better insight into these coherence properties, we analyze their dependence on the atom's driving strength. In resonance fluorescence, the light scattered by a quantum emitter consists of two types of photons belonging to either a coherently or an incoherently scattered component, which are emitted by the atom with the respective rates

$$n_{\text{coh}} = \gamma \frac{s}{(s+1)^2}, \quad (20)$$

$$n_{\text{inc}} = \gamma \frac{s^2}{(s+1)^2}, \quad (21)$$

where

$$s = \frac{\Omega^2}{2\gamma^2 + 2\Delta^2} = \frac{s_0}{1 + 2(\Delta/\gamma)^2} \quad (22)$$

with the on-resonance saturation parameter s_0 [45] and the detuning Δ between the atomic transition and the driving laser frequency. The total photon scattering rate of the atom is

$$n = n_{\text{coh}} + n_{\text{inc}} = \gamma \frac{s}{s+1}. \quad (23)$$

As coherently emitted photons possess a well-defined frequency and phase given by the laser frequency ω_0 , they exhibit a well-defined interference fringe that, in principle, has perfect visibility. In contrast, incoherent photons

exhibit a broad frequency distribution $\Delta\omega \geq (2\gamma)$ which is given by the Mollow-triplet [45]. For very long delays $\Delta t \gg (2\gamma)^{-1}$ in the unbalanced interferometer, the incoherent photons will thus not acquire a well-defined phase shift and consequently leave the interferometer with equal probability at each port, independent of the phase setting [46].

In order to obtain a prediction of the single-photon visibility we have to calculate the photon rates in the interferometer outputs which are given by

$$n_i(t) = \langle a_i^\dagger(t) a_i(t) \rangle, \quad (24)$$

where $i = 1, 2$ labels the two different outputs. These output fields are the sum of two fields from the two interferometers via $a_{1(2)}^\dagger(t) = (a_s(t) \pm e^{i\phi} a_l(t))/\sqrt{2}$. As these operators can be expressed in terms of the atomic raising and lowering operators σ^+ and σ^- , respectively, the photon output rate is given by

$$n_{1(2)} = \langle [\sigma^+(t + \Delta t) \pm e^{-i\phi} \sigma^+(t)] [\sigma^+(t + \Delta t) \pm e^{i\phi} \sigma^-(t)] \rangle. \quad (25)$$

Using the steady-state solutions from the optical Bloch equations together with the quantum regression theorem, the above expectation values can be calculated for our interferometer output modes. From these, we obtain for our experimental detuning of $\Delta = 2\pi \times 2.56$ MHz a saturation-dependent visibility shown in Fig. 6. In particular, for the driving strengths discussed in the manuscript, our theory predicts $V_{\text{theory}} = 97.6\%$ for low saturation ($s_0 = 0.10$) and $V_{\text{theory}} = 52.4\%$ for high saturation ($s_0 = 2.75$). We note that for high drive strengths we experimentally measure a higher visibility $V_{\text{exp}} = 61.8\%$. This discrepancy may originate from the different contributions of the individual experimental runs with fluctuating detuning to the averaged second-order correlation function (square of the scattered power) and the single photon interference fringes (linear in scattered power).

Using the above formalism also allows us to predict the two-photon expectation values for a large time delays δt . For $\delta t \rightarrow \infty$ the two-photon expectation simplifies to

$$\langle \sigma_{\phi_A} \sigma_{\phi_B} \rangle = \langle \sigma_{\phi_A} \rangle \langle \sigma_{\phi_B} \rangle. \quad (26)$$

D. Photon pair rate

The rate of photon pairs that can be detected in a coincidence window δt is given by

$$n_p = 2 \left(\frac{n}{2} \right)^2 \delta t = \frac{\gamma^2}{2} \frac{s^2}{(s+1)^2} \delta t. \quad (27)$$

If we use the characteristic time scale of the antibunching for the coincidence window, i.e., $\delta t = \frac{\tau}{2}$ with the atomic lifetime $\tau = (2\gamma)^{-1}$, the above expression simplifies to

$$n_p = \frac{\gamma}{8} \frac{s^2}{(s+1)^2} = \frac{1}{8} n_{\text{inc}}. \quad (28)$$

This expression shows that the entangled photon pair events detected in our experiment are, up to a factor, equal to the rate of emission of the incoherently scattered photons, thus shedding light onto their physical origin.

As the pair creation rate monotonously increases with the saturation of the atom, one good strategy to maximize the photon pair rate is to increase the atomic driving strength. However, stronger driving also narrows the antibunching interval in the second-order correlation function requiring adjustment of the coincidence window to obtain a high fidelity entangled state. To quantify the effect of this trade-off, we analytically derive the dependence of the antibunching window on the driving power as follows.

We consider on-resonance driving for which the second-order correlation function is given by [45]

$$g^{(2)}(\tau) = 1 - e^{-3\gamma\tau/2} \left(\cos \tilde{\Omega}\tau + \frac{3\gamma}{2\tilde{\Omega}} \sin \tilde{\Omega}\tau \right) \quad (29)$$

with the Rabi frequency Ω and $\tilde{\Omega}^2 = \Omega^2 - \gamma^2$. For high driving strengths, this function will oscillate with the Rabi frequency, resulting in a shorter time window in which photon antibunching can be observed. To get an analytical expression for this time window, we approximate the second-order correlation function around $\tau = 0$ by its Taylor expansion

$$g^{(2)}(\tau) \approx (2\gamma^2 + \Omega^2)\tau^2 + \dots \quad (30)$$

from which we get the power-dependent width of the antibunching window of

$$\delta\tau = \frac{1}{4}(\Omega^2/2 + \gamma^2)^{-1/2}. \quad (31)$$

Using this time window, together with Eq. (28), we obtain for the rate of entangled photon pairs

$$n_p = \frac{\gamma^2 \Omega^4}{16\sqrt{(\gamma^2 + \Omega^2/2)^5}}. \quad (32)$$

This expression has its maximum for $\Omega = 2\sqrt{2}\gamma$ or $s_0 = 4$ and reaches a value of

$$n_{p,\text{max}} = \frac{1}{25\sqrt{5}}\gamma \approx 0.02\gamma, \quad (33)$$

i.e., the maximum entangled photon pair rate reaches 2% of the maximum possible single photon scattering rate γ .

E. Trapping, detecting, and probing single atoms

We prepare a cloud of ^{85}Rb atoms inside an ultra-high vacuum chamber using a magneto-optical trap (MOT), that is used as a reservoir of cold atoms for loading an optical dipole trap. The dipole trap is generated by focusing a laser beam (wavelength: $\lambda = 784.65$ nm, waist radius: $w = 1.334 \pm 0.08$ μm) into the MOT cloud using a high

numerical aperture lens (AS-AHL12-10, Asphericon) (focal length: $f = 10$ mm, working distance: $w_d = 7.6$ mm) that is located inside the vacuum. Due to the microscopic trap volume, our trap operates in the collisional blockade regime [2, 47] such that, at most, a single atom is present inside the trapping volume at any time. For a laser power of $P = 0.58$ mW, we obtain an optical trapping potential with a depth of $U/k_B = 0.76$ mK, corresponding to trap frequencies of $\nu_r = 66.8$ kHz and $\nu_z = 9.1$ kHz in radial and axial directions, respectively.

Resonance fluorescence photons originating from the trapping volume are collected with the same in-vacuum lens, separated from the trapping light using a dichroic mirror (LL01-785-25, Semrock), and coupled into a single-mode fiber that also acts as a spatial filter. Photons in the fiber are detected using superconducting nanowire single photon detectors, SNSPDs (Eos R12, Single Quantum), with each arrival time recorded by an FPGA-based timetagging unit. The presence of an atom inside the dipole trap is registered by an increase in the detected photon rate from the background level of 500 s^{-1} to 3000 s^{-1} .

Following the detection of an atom in the dipole trap, an interleaved drive and cooling sequence is applied to the atom for a total duration of 200 ms. In the driving interval, we send a driving laser beam onto the trap region, which is resonant to the light-shifted transition of the atom and is applied perpendicular to the trap axis in order to minimize stray light. After this probing, we apply the cooling laser of the MOT to cool the atom back to its initial temperature. Each 500 μs cycle comprises a 60 μs drive interval followed by 440 μs of cooling at low saturation, or a 3 μs drive interval followed by 497 μs of cooling at high saturation. A repumping field remains constantly on during the sequence. The duration of the drive and cooling times were optimized by maximizing the total rate of fluorescence photons detected during the driving process. For a low-saturation driving, we detect a photon rate of 2.51 kHz, which agrees with the expected scattering rate under our low-excitation regime ($s_0 = 0.10$), when considering the limited collection efficiency of the lens and fiber ($\eta_0 \approx 1.2$ %), propagation losses through the Franson interferometer ($\eta_{\text{prop.}} \approx 20$ %), as well as the average SNSPD detector efficiency ($\eta_{\text{det.}} \approx 86$ %). Proportionally, for a high-saturation driving, we detect a photon rate of 26.44 kHz, showing a high-saturation driving strength with $s_0 = 2.75$.

F. Fiber-based Franson interferometer

Our Franson interferometer consists of two unbalanced Mach-Zehnder interferometers constructed using optical fibers spliced to commercially available 50 : 50 fiber beamsplitters (TN785R5A2, Thorlabs). The long arm of each interferometer includes a home-made piezo-based fiber-stretcher to control the interferometer phases ϕ_A and ϕ_B . The whole setup is placed inside a thermally-

insulated box with typical temperature stability of better than 0.1°C on a daily time scale. The optical path length difference between the long and short arms in each interferometer, $\Delta L_{A(B)}$, is measured by injecting a ~ 1 ns duration pulse of light (wavelength: $\lambda \approx 780$ nm) into the Franson interferometer and monitoring its arrival time on each output using the four SNSPDs. From the observed delay time $\Delta t_A = 46.1 \pm 0.2$ ns and $\Delta t_B = 46.7 \pm 0.2$ ns, we calculate respective path length differences of $\Delta L_A = 9.50 \pm 0.004$ m and $\Delta L_B = 9.63 \pm 0.004$ m.

To ensure a polarization-independent operation of the interferometers, fiber birefringence is compensated by using in-line polarization controllers (CPC900, Thorlabs) in each interferometer to maximize the fringe visibility for orthogonal input polarizations. Following this procedure, we measure a visibility of 99 ± 1 % in each interferometer averaged over four different polarizations of the input light (linear vertical and horizontal, left- and right-circular). The uncertainty in this estimation mainly comes from the background noise of the photodetectors.

During the experiment, each interferometer is set to impart a desired phase shift on the transmitted light. These phases are set by fixing the length of the long arm in each interferometer following a sample-and-hold locking procedure, which takes place every 30 s. During a locking cycle, the driving light is injected into the Franson interferometer. An error signal is obtained by monitoring the difference in the count rate at the two outputs of each interferometer. To lock to the desired phase shift, a frequency shift is applied to the lock laser to move the zero-crossing of the error signal to the desired path length difference. Between locking cycles, the interferometer was free running with a maximal drift rate of the interferometer phase (likely due to slow thermal fluctuations) of about $2\pi \times 0.022 \text{ rad min}^{-1}$.

G. Analysis of measured correlation data

Anticorrelations in the light scattered by single atoms are measured using an HBT set-up, in which the output of the fluorescence collection fiber is connected to a 50 : 50 fiber beamsplitter with an SNSPD at each output (Fig. 2b). Coincidence events were recorded in cycles following the same sequence as the CHSH measurement. In addition, the data exhibits a slow bunching envelope on the microsecond timescale, arising from atomic heating during driving.

To account for this, we fit the function $1 + Ae^{-|\tau|/t_b}$ to the coincidence data for large time delays. The value $1 + A$ then serves as the baseline. After normalisation we observe $g^{(2)}(0) = 0.05 \pm 0.036$ for $s_0 = 0.10$ and $g^{(2)}(0) = 0.069 \pm 0.048$ for $s_0 = 2.75$. The fits shown in Fig. 2b are based on the second-order correlation function of a two-level atom, taking into account a distribution of atom-light detunings to account for the different AC Stark shifts experienced by the atom due to its finite temperature in the trap. The fit yields a mean resid-

ual detuning of the atomic resonance to the drive field of $\Delta/2\pi = 2.56 \pm 0.16$ MHz.

H. Maximum likelihood estimation

The density matrix displayed in Fig. 5 is reconstructed using a maximum likelihood estimation (MLE) method [48, 49]. For this, we define a physical density matrix ρ as

$$\rho = \frac{T^\dagger T}{\text{Tr}(T^\dagger T)} \quad (34)$$

where T is a 4×4 lower triangular complex matrix with free parameters that guarantee ρ is positive, semidefinite and normalized.

Each measurement setting, labeled by the indices ij , is described by a two-outcome positive operator-valued measure (POVM) with the projection operator

$$P_\pm^{ij} = \frac{I \pm \langle \sigma_i \sigma_j \rangle}{2}. \quad (35)$$

For a set of measurements $\{P_+^{ij}, P_-^{ij}\}$, we can define the likelihood function by

$$L(\rho) = \prod_{ij} \left[\text{Tr}(\rho P_+^{ij}) \right]^{n_+^{ij}} \left[\text{Tr}(\rho P_-^{ij}) \right]^{n_-^{ij}}, \quad (36)$$

where $n_+^{ij} = n_{a_1, b_1} + n_{a_2, b_2}$ and $n_-^{ij} = n_{a_1, b_2} + n_{a_2, b_1}$ are the number of detection events that yielded the outcomes $+1$ and -1 for the measurement $\langle \sigma_i \sigma_j \rangle$, respectively. Taking the natural logarithm of $L(\rho)$, we obtain

$$\mathcal{L}(\rho) = \sum_{ij} \{ n_+^{ij} \ln [\text{Tr}(\rho P_+^{ij})] + n_-^{ij} \ln [\text{Tr}(\rho P_-^{ij})] \}. \quad (37)$$

Introducing the total number of detected coincidences $N_{ij} = n_+^{ij} + n_-^{ij}$ we rewrite the above equation and obtain the likelihood function as

$$\begin{aligned} \mathcal{L}(\rho) = \sum_{ij} \frac{N_{ij}}{2} \{ (1 + \langle \sigma_i \sigma_j \rangle) \ln [\text{Tr}(\rho P_+^{ij})] \\ + (1 - \langle \sigma_i \sigma_j \rangle) \ln [\text{Tr}(\rho P_-^{ij})] \}. \end{aligned} \quad (38)$$

I. Reconstruction of the density matrix

To reconstruct the density matrix, we perform measurements with the phase settings $(\phi_A, \phi_B) =$

$(0, 0), (0, \frac{\pi}{2}), (\frac{\pi}{2}, 0)$ and $(\frac{\pi}{2}, \frac{\pi}{2})$. The measured expectations and coincidences are summarized in Table I.

To realize a full quantum tomography, measurements in all bases $\{\sigma_i \otimes \sigma_j\}$ ($i, j = x, y, z$) should be performed. In our setup, direct measurements of expectation values involving the operator σ_z are infeasible, since it would

TABLE I. Measurement for density matrix reconstruction

projection	Expectations $\langle \sigma_i \sigma_j \rangle$	Total coincidences N_{ij}
$\sigma_x \otimes \sigma_x$	0.679	112
$\sigma_x \otimes \sigma_y$	0.018	110
$\sigma_y \otimes \sigma_x$	0.083	133
$\sigma_y \otimes \sigma_y$	0.928	138

require disassembling the interferometer. Instead, we exploit the fact that the z -basis is the natural basis of the system. The expectation value $\langle \sigma_z \sigma_z \rangle$ can thus be determined from the probabilities of finding the photons in the four path configurations $|s, s\rangle, |s, l\rangle, |l, s\rangle$ and $|l, l\rangle$, where $|s\rangle$ and $|l\rangle$ represent photons in the short or long interferometer arms, respectively. As these probabilities are defined by the quality of the measured photon antibunching, we can extract the expectation value from evaluating the measured second-order correlation functions at time $\tau \in [-\delta t, \delta t]$ and at a time $\Delta t + \tau$, yielding

$$\langle \sigma_z \sigma_z \rangle = - \int_{-\delta t}^{\delta t} d\tau \left(1 - \frac{\sum g^{(2)}(\tau)}{\sum g^{(2)}(\tau + \Delta t)} \right), \quad (39)$$

where Δt is the interferometer's path delay. The correlations $\langle \sigma_z \sigma_x \rangle$ and $\langle \sigma_z \sigma_y \rangle$ cannot be obtained in this way and are set to zero in our reconstruction, as they are absent in the expected state and their value has no impact on the fidelity of the reconstructed density matrix.

The density matrix ρ in Fig. 5 is reconstructed by minimizing the negative log-likelihood $-\mathcal{L}(\rho)$ in Eq. (38), with ρ parameterized as Eq. (34) to ensure physicality. Numerical optimization is performed via Mathematica's `FindMinimum` with the `QuasiNewton` method. For the fidelity of the generated Bell state we obtain $F = \langle \Psi_{\text{Bell}} | \rho | \Psi_{\text{Bell}} \rangle = 0.87 \pm 0.02$. Here, the statistical error is determined using a Bootstrap method, where we add Poissonian noise to the measured coincidences and followed by the density matrix reconstruction. For this, we generate a set of 100 random density matrices and use the resulting standard deviations as error estimation.

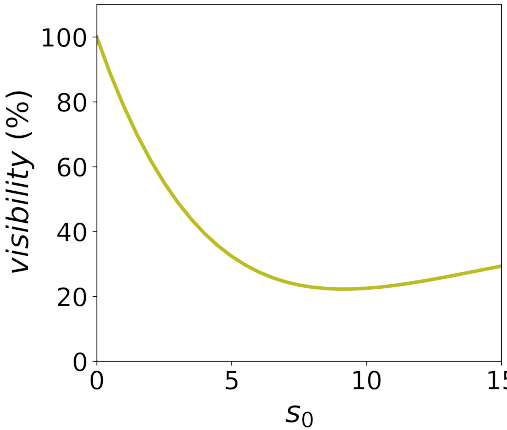


FIG. 6. **Theoretically calculated single-photon visibility versus saturation parameter.** Theoretical prediction of single-photon interference visibility V as a function of the driving saturation parameter s_0 , for our experimental parameters, see section C in the Supplementary Materials.